Lessons learnt on the impact of an unprecedented soil decontamination program in Fukushima on contaminant fluxes

Rosalie Vandromme, Seiji Hayashi, Thomas Grangeon, Hideki Tsuji, Olivier Evrard, Valentin Landemaine, John Patrick Laceby, Yoshifumi Wakiyama, Olivier Cerdan

PNAS RESEARCH ARTICLE | ENVIRONMENTAL SCIENCES OPEN ACCESS

Lessons learnt on the impact of an unprecedented soil decontamination program in Fukushima on contaminant fluxes

Rosalie Vandromme[a,1], Seiji Hayashi[b], Hideki Tsuji[b], Olivier Evrard[c], Thomas Grangeon[a], Valentin Landemaine[a], John Patrick Laceby[c,d], Yoshifumi Wakiyama[e], and Olivier Cerdan[a]

Edited by Susan Brantley, Pennsylvania State University, University Park, PA; received February 2, 2023; accepted September 8, 2023

In the context of elevated concerns related to nuclear accidents and warfare, the lessons learnt from the Fukushima Daiichi Nuclear Power Plant accident in 2011 are important. In particular, Japanese authorities implemented an ambitious decontamination program to reduce the air dose rate in order to facilitate the return of the local inhabitants to previously evacuated areas. This approach contrasts the strategy adopted in Chernobyl, where the most contaminated areas remain off limits. Nonetheless, the effectiveness of the Japanese decontamination strategy on the dispersion of radioactive contaminant fluxes across mountainous landscapes exposed to typhoons has not been quantified. Based on the unique combination of river monitoring and modeling in a catchment representative of the most impacted area in Japan, we demonstrate that decontamination of 16% of the catchment area resulted in a decrease of 17% of sediment-bound radioactive fluxes in rivers. Decontamination operations were therefore relatively effective, although they could only be conducted in a small part of the area due to the dominance of steep forested slopes. In fact, 67% of the initial radiocesium contamination was calculated to remain stored in forested landscapes, which may contribute to future downstream radiocesium dispersion during erosive events. Given that only a limited proportion of the initial population had returned in 2019 (~30%), it raises the question as to whether decontaminating a small percentage of the contaminated area was worth the effort, the price, and the amount of waste generated?

soil erosion | particulate ^{137}Cs | erosion modeling | decontamination | Fukushima Daiichi accident

Significance

We used a combined experimental-modeling approach to study soil erosion, sediment, and Cesium-137 (^{137}Cs) transfers in a representative catchment contaminated by the radioactive fallout from the Fukushima Daiichi Nuclear Power Plant accident. This study disentangled and evaluated the processes of ^{137}Cs transfers in a landscape that was included in the early decontamination program performed by the Japanese authorities following the accident. The model demonstrates that the decontamination program was effective in the treated areas, though 67% of the initial radiocesium remains in forested landscapes. The persistence of ^{137}Cs in forests remains an obstacle to the return of the local inhabitants and the resumption of economic activities associated with forest exploitation.

Contamination from nuclear accidents and warfare have multiple negative impacts on the environment and society (e.g., human health and population migration). Following the Fukushima Daiichi Nuclear Power Plant (FDNPP) accident in March 2011, the Japanese authorities implemented an ambitious decontamination program, which strongly differs from the strategy adopted in Chernobyl where the most contaminated areas still remain off limits. The increasing likelihood of natural disasters with climate change (e.g., extreme events such as droughts, heatwaves, heavy rainfalls, and floods), in addition to seismic risk, may result in other unanticipated nuclear accidents. Unfortunately, the question of decontamination verses restricting access to contaminated areas after a nuclear accident is likely to arise again. Therefore, tools that can help design mitigation strategies to reduce the effects of radioactive fallout are urgently needed.

The FDNPP accident resulted in a massive release of radioactive contaminants into the atmosphere. Although 80% of the fallout from this atmospheric release occurred over the ocean, the remaining 20% was deposited on land in Japan (1–3). One of these radioactive contaminants, cesium-137 (^{137}Cs) is considered to be the most serious risk to the local population because it was emitted in high abundance and it has a relatively long half-life of 30 y (4, 5). Once ^{137}Cs reaches the soil surface, it is quickly and almost irreversibly bound to fine soil particles (6–8) and therefore remains in the upper few centimeters of the soil profile, with very limited vertical migration (9). Research conducted on soil profiles collected in Fukushima Prefecture after the 2011 accident demonstrated that 95% of the ^{137}Cs in the soil is strongly bound to clay materials (10) and concentrated in the upper 2 cm of undisturbed soils (11, 12), making it susceptible to downstream transfer by water erosion during rainfall events. After the FDNPP accident, ^{137}Cs has been shown to have been transported mainly with suspended matter in rivers draining the main radioactive plume (13–17).

The amount of radiocesium that is washed away by water erosion on hillslopes depends on its concentration in the soil, which is the result of the initial radiocesium fallout concentration, and the magnitude of soil loss driven by local erosion processes (16). Climate and extreme weather events represent key factors driving ^{137}Cs transfers in catchments with annual variations depending on climate seasonality, as river transfers increase in response to heavy rainfall during summer typhoons and spring snowmelt.

Author contributions: R.V., S.H., O.E., T.G., J.P.L., and O.C. designed research; R.V., S.H., H.T., O.E., T.G., V.L., J.P.L., Y.W., and O.C. performed research; R.V., T.G., and V.L. contributed new reagents/analytic tools; R.V., S.H., T.G., and V.L. analyzed data; and R.V. and S.H. wrote the paper.

The authors declare no competing interest.

This article is a PNAS Direct Submission.

[1]To whom correspondence may be addressed. Email: r.vandromme@brgm.fr.

This article contains supporting information online at https://www.pnas.org/lookup/suppl/doi:10.1073/pnas.2301811120/-/DCSupplemental.

Published October 16, 2023.

Several studies in the Fukushima region have demonstrated that a single typhoon can account for a large portion of the annual ^{137}Cs export (13, 14, 17, 18). In addition to the major role played by rainfall erosivity (19), topography, land use and soil characteristics also greatly affect the local spatial patterns of erosion and sediment deposition (16). In particular, the area of the main radioactive plume is mainly covered with forests on steep slopes and agricultural land in the valley bottoms, including paddy fields. Erosion rates on agricultural land are much greater than those under grassland and forests. Consequently, cropland is the main source of sediment and radiocesium fluxes in this area (17, 20).

This knowledge of the initial spatial pattern of the radioactive contamination across the landscape and the main redistribution processes has guided the Japanese authorities in their choices to implement a remediation strategy. A decontamination roadmap was established in January 2012 under the direct supervision of the Japanese government. The decontamination program was implemented in special areas where targets were set with regard to the exposure of the public to air dose rates that would allow residents to return to their day-to-day lives. These areas were mainly residential, including zones located within a radius of 20 m around houses and roads or cultivated areas (mainly paddy fields). Forests were not targeted because the implementation of decontamination is technically complicated and less efficient in these areas (e.g., removal of litter and humus) and they are expected to be less susceptible to erosion.

The original goal of the decontamination work in Fukushima was accomplished, as the air dose rates in living areas were reduced by 30 to 50% on average, thus allowing residents to return (21). ^{137}Cs concentrations in sediment transported in river systems draining the main radioactive plume were also shown to have significantly decreased between 2011 and 2020 (22–25). This is due to the cumulated effects of ^{137}Cs physical decay, erosion, and decontamination operations. Although the relative proportion of these different processes cannot be experimentally quantified, novel modeling tools can be developed to estimate these dynamic processes (Table 1). The fact that ^{137}Cs remains elevated in river systems shows that forests continue to provide a significant contribution to ^{137}Cs fluxes (20).

These post-accidental conditions, including the completion of a large-scale decontamination program, provide an opportunity to quantify the impacts of the decontamination program on erosion, ^{137}Cs fluxes, and the remaining ^{137}Cs stock. Quantification and understanding of the physical processes involved in particulate ^{137}Cs transfer can provide a fundamental scientific foundation to help policymakers make decisions in the event of another nuclear catastrophe. Accordingly, the objectives of this study are to i) design and validate an original radiocesium module with a spatially distributed runoff, erosion model, ii) analyze ^{137}Cs flux monitoring data and rainfall data acquired during the decontamination operations, and iii) evaluate the potential fluxes and stocks without decontamination, simulating the approach taken in Chernobyl.

Results

Study Region and Decontamination Strategy. The study catchment (44 km^2) is a headwater mountainous watershed representative of those found in the main radioactive plume in the Fukushima Prefecture, Northeastern Japan. It is drained by the Mano River and located upstream of the Mano Dam (Lake Hayama). The Mano Dam catchment is in the northern part of the radioactive contamination plume of the FDNPP and drains soils with total initial ^{137}Cs concentrations ranging from 3,500 to 17,500 Bq kg^{-1} (Fig. 1) (28). In this northern area, upstream sections of the catchments are the most contaminated with ^{137}Cs. The catchment's elevation varies from 180 m to 694 m, and approximately 50% of the catchment has a slope >25°. The Mano Dam catchment is mainly covered with forests (88.0%), residential areas (5.6%), agricultural land (3.3%), ponds and streams (2.3%), and roads (0.7%). Further downstream in the study catchment, toward the coastal plain, the proportion of agricultural land increases, at the expense of woodland.

A hydrological station installed immediately upstream of Mano Dam Lake was used to measure water flows and sediment concentrations at 5-min intervals from June 2014 to September 2015. The hydrological station was moved a few hundred meters further upstream in 2017 because of damage from Typhoon Etau. Flow and sediment concentrations were subsequently monitored at 10-min intervals until the end of 2019 (*SI Appendix*,

Table 1. Summary table of previous studies addressing particulate ^{137}Cs fluxes monitoring and modeling in the Fukushima region

			Monitoring				Modeling			
References	Period	Location	Q	SSC	^{137}Cs–p	D	Q	SSC	^{137}Cs–p	D
(4)	Use of data from 2000 to 2010 to make predictions	Abukuma River catchment	X				X	X	X	
(13)	2013, 2015 and 2016	Hiso River and Mano River catchments	X	X	X	X				
(14)	2011 to 2012	Abukuma River catchment	X	X	X		X	X	X	
(16)	July 2011 to Nov 2012	Plots (5 m × 22.1 m) in Kawamata Town	X	X						
(15)	2011 to 2100	Abukuma, Uta, Mano, Niida, Ota, Odaka, Ukedo, Maeda, Tomioka, Ide, Kido, Natsui and Same rivers catchments					X	X	X	
(26)	Jan 2011 to Dec 2012	Kuchibuto River catchment	X	X	X		X	X	X	
(27)	May 2011 to Dec 2015	Oginosawa River catchment	X	X	X		X	X	X	
(23)	2013 to 2018	Niida River catchment		X	X	X		X		X
This study	Jun 2014 to Dec 2019	Mano Dam catchment	X	X	X	X	X	X	X	X

Q = discharge, SSC = suspended sediment concentration, ^{137}Cs–p = particulate ^{137}Cs, D = impact of decontamination works.

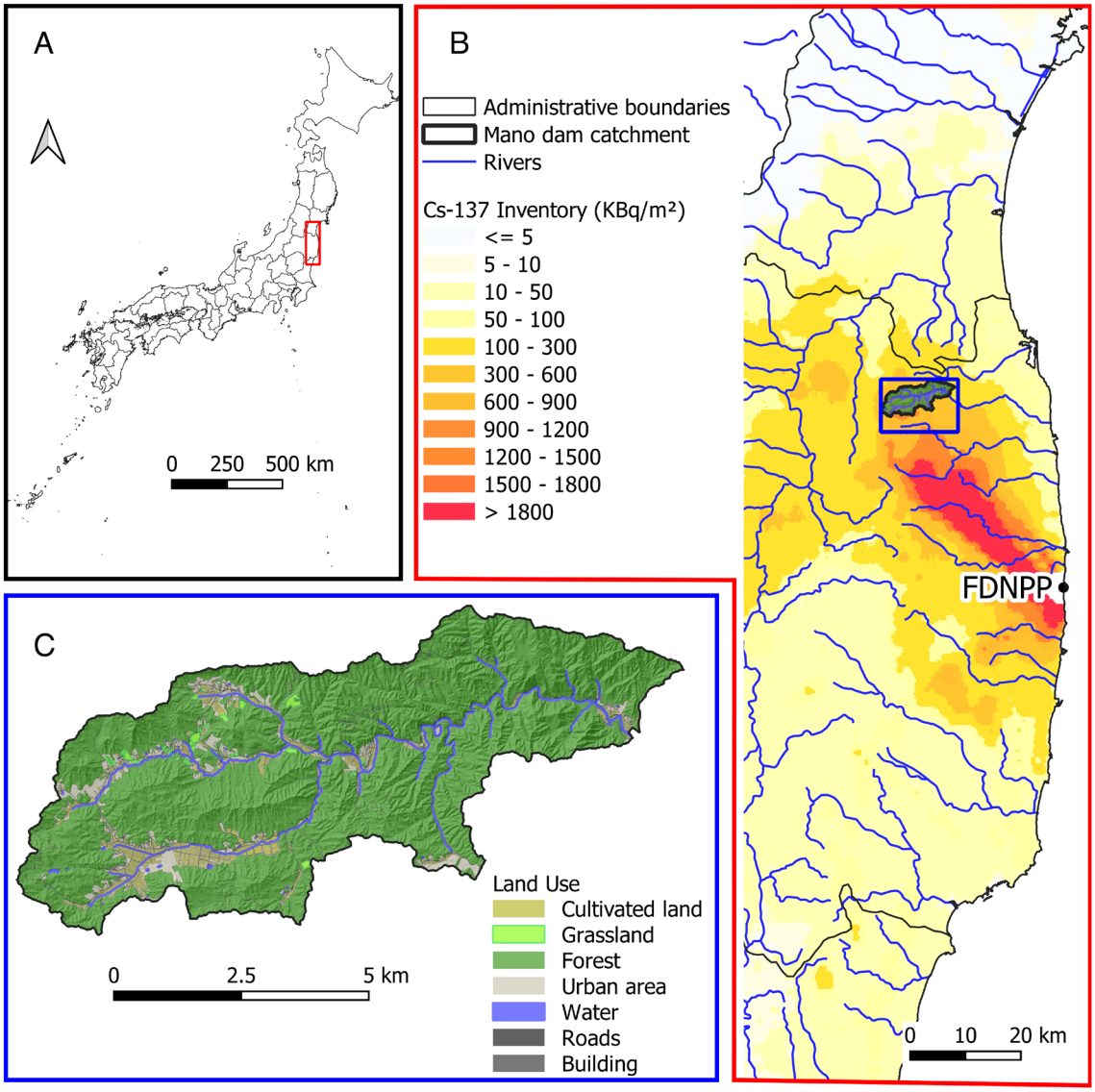

Fig. 1. Location of the studied catchment in Japan and representation of the main radioactive plume just after the FDNPP accident. (*A*) Location of the study area (red rectangle) in Japan. (*B*) Representation of the reconstructed initial ^{137}Cs fallout map (29), including the main rivers (blue line) and the studied catchment (blue rectangle). (*C*) The headwater Mano Dam catchment land use type overlying a shaded relief map.

Fig. S6). Moreover, river water samples were collected to measure ^{137}Cs concentration in suspended sediment (SS) (66 measurements during floods, *SI Appendix*, Fig. S6) from June 2014 to December 2019 (30). A rainfall record acquired by the Fukushima Prefecture was available for this catchment (Maenori station) at 10-min time steps during the entire hydrological monitoring period (30).

In the Mano Dam catchment, decontamination operations occurred between June 2014 and December 2016 (*SI Appendix*, Fig. S7). The decontaminated area progressively increased from 7.7 ha in 2015 to 54 ha in early 2016 and was ultimately implemented on an area of 700 ha by early 2017 (16% of the total catchment area). Decontamination operations consisted of the removal of vegetation and the replacement of topsoils (within the upper ~5 cm) with locally extracted crushed rock (granite or sandstone) (31). After decontamination, residual ^{137}Cs activities in soils were estimated to reach a maximum of 20% of the initial activity levels (32) and the erodibility and potential sediment concentrations in runoff from farmlands increased significantly. Areas decontaminated in winter remained more erodible during this period as soils were left bare and exposed to rainfall, runoff, and erosion. During the rest of the year, due to vegetation growth, erodibility of decontaminated areas decreased within 2 mo.

Measured Suspended Sediment and ^{137}Cs Concentrations at the Catchment Outlet. Point-based ^{137}Cs concentrations at the outlet of the catchment from June 2014 to the end of 2019 during storm flow events were analyzed against flow rate (in Bq L^{-1}) and suspended sediment concentration (SSC) (in Bq g^{-1}) to investigate potential relationships with erosion processes and decontamination operations (Fig. 2). The measured particulate ^{137}Cs concentrations in SS decreased exponentially over time (Fig. 2*A*), as a result of ^{137}Cs physical decay, erosion, and decontamination operations. The relative proportion of these different processes cannot be experimentally quantified. Scattering is found in the regression plots, which is the result of cumulative changes in sediment source contributions, uncertainties in SS monitoring (33) and annual fluctuations in ^{137}Cs concentrations (24).

The Fig. 2*B*–*D* show the occurrence of two different trends before 2016 during and after the decontamination operations.

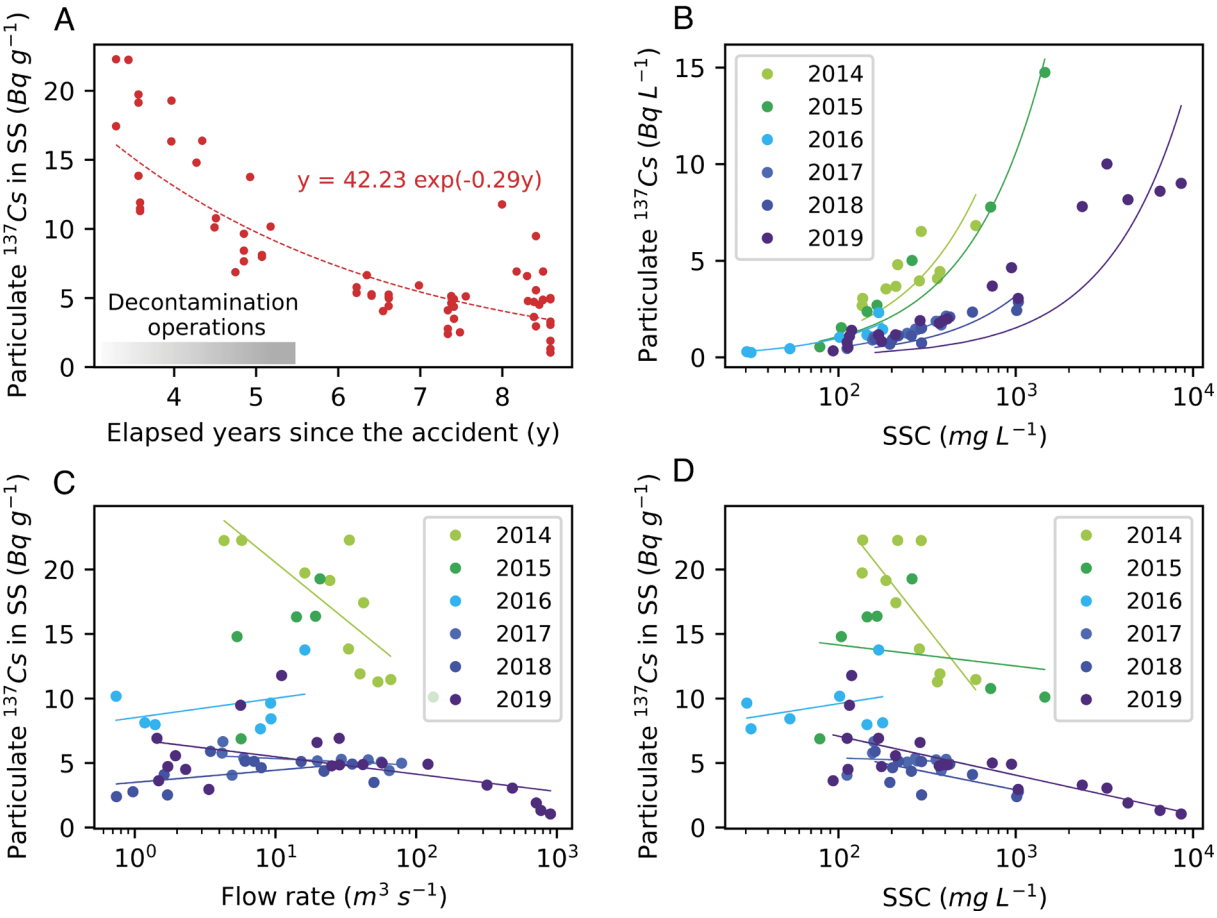

Fig. 2. Point-based particulate ^{137}Cs concentration measurements in SS sampled at the outlet of the Mano Dam catchment from June 2014 to the end of 2019 during storm flow events. (*A*) Particulate ^{137}Cs concentrations in SS (in Bq g^{-1}) vs. elapsed years since the accident and corresponding exponential fitted curve (the gray bar above the *x* axis indicates the duration of decontamination operations). (*B*) Particulate ^{137}Cs concentrations (in Bq L^{-1}) vs. SSC. (*C*) Particulate ^{137}Cs concentrations (in Bq g^{-1}) vs. flow rate. (*D*) Particulate ^{137}Cs concentrations (in Bq g^{-1}) vs. SSC. In *A*–*C* trend lines/curves each correspond to the measurement points for 1 y. The color gradient from green to purple indicates the sampling years.

Before 2016, ^{137}Cs concentrations are high even for low sediment concentrations and low flow rates. After 2016, ^{137}Cs concentrations are in contrast lower on average and for a wide range of conditions.

Point-based measurements of ^{137}Cs concentrations illustrate that the higher the SSC, the lower the ^{137}Cs concentration in SS (Fig. 2*D*). This finding suggests an erosion dilution effect during intense rainfall and flood events. The most intense events can generate rill (or gully) erosion that incises the soil profile and therefore mobilizes subsoil. Indeed, large gullies were observed on steep forested slopes, at several locations across the catchment area. Rill or gully erosion processes can release large amounts of sediment, particularly from subsoils deeper than the FDNPP ^{137}Cs contamination (e.g., a few centimeters). During less intense rainfall events, inter-rill erosion dominates and mobilizes surface soil particles enriched in ^{137}Cs. These results confirm previous findings (13) obtained for the Mano and Hiso River catchments between 2013 and 2016, and more importantly, validate these results over a longer time frame (until 2019), providing a strong basis for modeling and process analysis.

Modeled Sediment Dynamics and Fluxes. The WaterSed model was used to model runoff, erosion, and associated ^{137}Cs fluxes. It is an event-based distributed model that simulates runoff and soil erosion from the plot to the catchment scale during a sequence of rainfall events (34–37). It is a raster-based model that describes runoff, erosion, and sediment transport based on hydrological and sediment balances. Infiltration-excess and saturation-excess runoff are included, as well as sheet and gully erosion—see *SI Appendix* for more details. The model was calibrated and validated with the measured flow rate and suspended sediment data: 21 events between June 2014 and September 2015 were used for calibration and an extensive set of 103 events between June 2014 and December 2019 were used for validation. Soil erosion properties in decontaminated areas (from June 2014 to December 2016) were increased following decontamination operations and then gradually decreased following vegetation regrowth.

To quantify and analyze particulate ^{137}Cs transfer and sources, we modeled all the rainfall events that occurred from June 2014 to December 2019 (296 events, Fig. 3). The calculation of the water runoff volume and the total sediment exports over the entire monitoring period permitted the determination of a specific sediment yield of 1 t ha^{-1} y^{-1}, which is in good agreement with results from similar Japanese catchments (4, 13, 14, 16, 38). Despite representing 0.24% of the monitoring period, five typhoon events represented 37% and 50% of water and sediment fluxes measured at the catchment outlet, respectively, underlining the importance of extreme events driving sediment dynamics in this region (31, 37).

The spatial analysis of the sediment quantities eroded by rill or inter-rill erosion for each land use type shows that the primary sediment source is rill/gully erosion in forests (~60%), followed by inter-rill erosion in forests (~20%), and paddy fields (~14%)

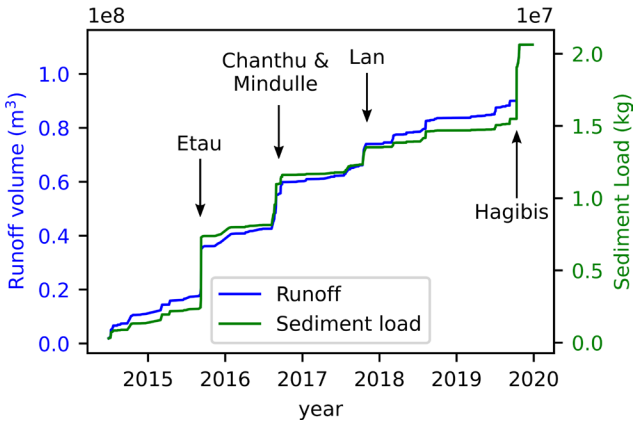

Fig. 3. Modeling results from June 2014 to the end of 2019. Cumulative water runoff volume (in blue) and sediment load (in green) at the catchment outlet. The arrows indicate the main typhoons that occurred during the monitoring period.

(Fig. 4*A*). Inter-rill erosion in grassland, urban areas, and residential areas was less significant. Notably, our findings suggest that in forests, rill erosion can occur during moderate to heavy rainfall. In contrast, inter-rill erosion in forests occurs only during major events (e.g., typhoons).

The WaterSed model has been calibrated (*SI Appendix*, Fig. S2) and validated (*SI Appendix*, Fig. S4) based on the monitoring dataset. It correctly reproduces the dynamics and sediment fluxes generated by the rainfall events of the 2014 to 2019 period (see *Material and Methods* for more details), which includes the decontamination phase.

Designing and Calibrating a ^{137}Cs Module. A radiocesium module was designed and added to the WaterSed model that adequately reproduced runoff and sediment fluxes to simulate particulate ^{137}Cs transport as well. This module is based on the following assumptions: i) ^{137}Cs is transported in particulate form only, ii)^{137}Cs resulting from post-accident fallout was deposited over a constant soil thickness, iii) a constant bulk density value of 1,400 kg m^{-3} was assumed for soils of the region, and iv) the activity concentrations are decay-corrected to the date of the accident.

The model was initialized with a constant contaminated soil thickness and a corresponding ^{137}Cs soil concentration map. The ^{137}Cs inventory and associated contaminated soil thickness are updated following erosive rainfall events. After each run, ^{137}Cs inventory and associated contaminated soil thickness maps are used to calculate the updated catchment total ^{137}Cs stock.

The radiocesium module was calibrated using the same 21 events outlined above for the WaterSed model, using the soil-contaminated depth as a calibration parameter. The best results obtained for the ^{137}Cs fluxes at the outlet were found for a soil contamination depth of 2.2 cm (*SI Appendix*, Fig. S2*D*). The radiocesium module was then validated on 103 events that took place between June 2014 and December 2019 (*SI Appendix*, Fig. S4*D*).

All the rainfall events that occurred from June 2014 to December 2019 were then modelled. As found previously for the sediment fluxes, the majority of ^{137}Cs exports occur during typhoons (Fig. 5*A*), although the relative contributions of radiocesium sources are different (Fig. 4*C*). The primary source of radiocesium is inter-rill erosion in forests (~50%) followed by inter-rill erosion in paddy fields (30%). Inter-rill erosion in residential areas and rill erosion in forests each contributed 9%.

Impact of Decontamination on Modeled ^{137}Cs Fluxes and Stocks. We used the decontamination program data, the associated measurements, and the development of the ^{137}Cs transfer module to provide an estimate of the relative contribution of the natural ^{137}Cs decay, decontamination operations, and particle transport in river systems during erosive rainfall events to the total ^{137}Cs fluxes and stock variations. To quantify the relative contribution of the decontamination operations, the model was run with and without decontamination. The impact of decontamination operations on sediment exports (~3 tons) was found to be negligible compared to the total quantities exported downstream (~20,000 tons). Indeed, after decontamination, the soil remains bare for a very short period of time due to the rapid regrowth of vegetation, which protects it from erosion. However, decontamination operations had a significant impact on the relative contributions of radiocesium sources (Fig. 4*B* and *C*), ^{137}Cs fluxes (Figs. 5*A* and 6), and catchment ^{137}Cs total stock (Fig. 5*B*). Without decontamination (Fig. 4*B*), the results of the model demonstrate that the primary sources of radiocesium would be inter-rill erosion in paddy fields (~40%) and forests (~40%) followed by inter-rill erosion in residential areas (~10%) and rill erosion in forests (~7%).

Over the entire period (mid 2014 to 2019), the basin has exported 0.24 TBq of particulate ^{137}Cs (Fig. 5*A*). Without decontamination, these exports would have amounted to 0.29 TBq. Hence, the decontamination implemented on 16% of the catchment surface area reduced the ^{137}Cs flux in rivers by only an

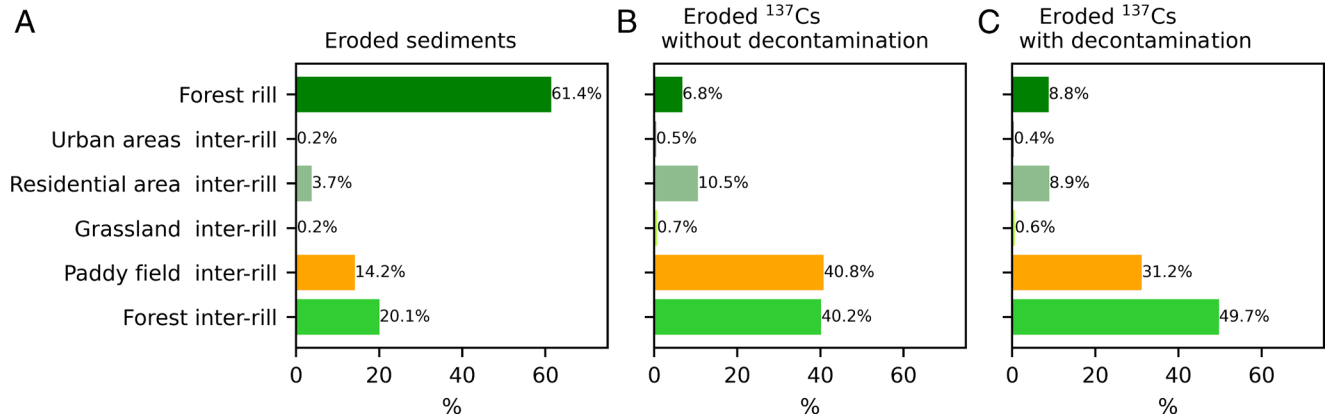

Fig. 4. Modeled sources proportions (%), according to land use and erosion type (i.e., rill or inter-rill erosion), of (*A*) eroded sediments including decontamination operations, "eroded" radiocesium (*B*) without decontamination, and (*C*) with decontamination.

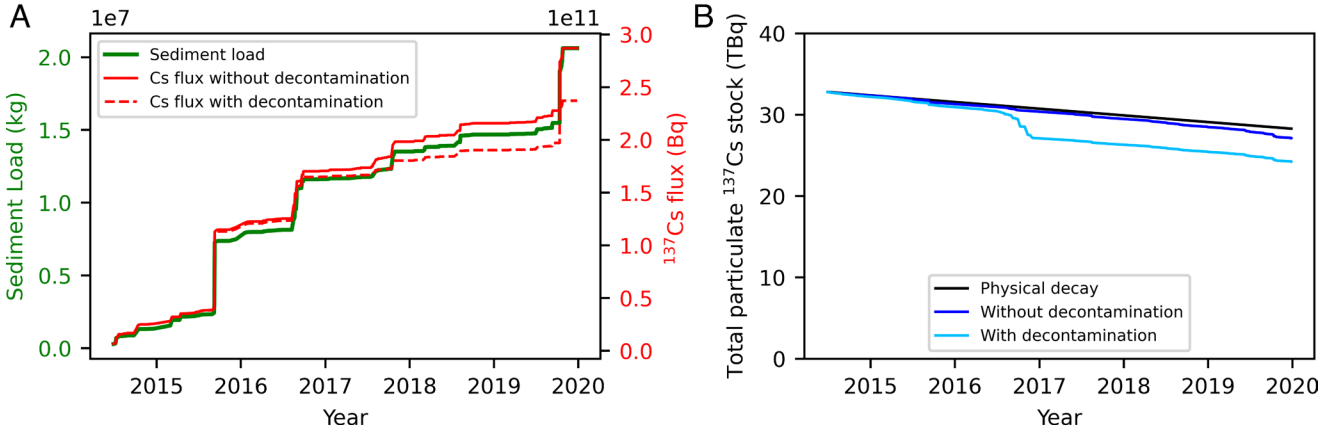

Fig. 5. Modeling results from June 2014 to the end of 2019. (*A*) Cumulated sediment load (in green) and particulate ^{137}Cs flux with (red dotted line) and without (red line) decontamination operations (in red) at the catchment outlet. (*B*) Mano Dam catchment particulate ^{137}Cs soil stock evolution with i) decontamination and erosion (Cyan), ii) without decontamination and with erosion (blue), and iii) without decontamination and without erosion (black).

additional 17% compared to that estimated in the absence of any decontamination measure.

The simulated ^{137}Cs concentrations in sediment transported in late 2019, after decontamination had been completed in the area, incorporating the decontamination work in the calculations (2,500 Bq kg^{-1}), were close to the measured values (less than 5,000 Bq kg^{-1}) (Fig. 6). In contrast, the simulations without decontamination were three times higher (7,500 Bq kg^{-1}) than the measured values.

The initial ^{137}Cs stock in the catchment immediately after the accident in 2011 was estimated to be 37.1 TBq. This stock was estimated to be 32.8 TBq at the time when monitoring started in 2014, taking into account the physical decay of ^{137}Cs and the 1.5% decrease in the initial inventory through riverine exports from 2011 to 2014. The estimated ^{137}Cs stock taking decontamination operations into account was found to reach 24.2 TBq by 2019, representing a 26% decrease in the ^{137}Cs stock compared to that in 2014. (Fig. 5*B*). The estimated ^{137}Cs stock without decontamination was modeled to reach 27.1 TBq by 2019, representing a 17% decrease in the ^{137}Cs stock compared to that in 2014. If we only apply decay correction from 2014 onward, the stock would be 28.3 TBq in 2019, corresponding to a decrease of 13.5% compared to the stock in 2014 (Fig. 5*B*).

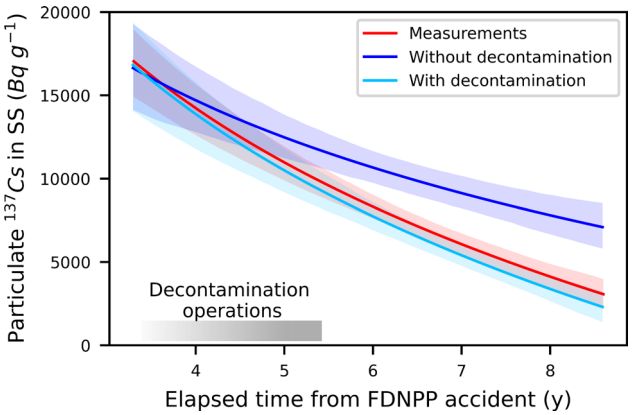

Fig. 6. Fitted particulate ^{137}Cs concentrations in SS (exponential) for measured, modeled with and without decontamination data (red, cyan, and blue, respectively) vs. elapsed time from FDNPP accident. The shaded areas represent the 95% CIs. The duration of decontamination operations is indicated by the gray bar above the *x* axis.

Accordingly, soil erosion reduced the catchment ^{137}Cs stock by a further 3.5% and decontamination operations reduced the catchment by an additional 9% (2.9 TBq). Of note, the average maximum riverine flux was found to be 0.05 TBq y^{-1}, which remains negligible (0.1%) compared to the initial stock of ~37 TBq of ^{137}Cs deposited in the catchment and is also very low (0.5%) compared to the stock remaining after decontamination (~25 TBq). Although typhoons clearly have a major impact on ^{137}Cs riverine fluxes, as shown in Fig. 5*A*, during the heaviest rainfall events, these exports are on the order of 0.1 TBq, which is very low compared to the total ^{137}Cs stock in the catchment (~37 TBq). Accordingly, these events had only a very limited impact on the reduction in the total ^{137}Cs stock (Fig. 5).

Discussion

The original goal of the decontamination work in Fukushima was accomplished, as the air dose rates in living areas (i.e., in farmland and residential areas, not in surrounding forests) were reduced by 30 to 50% on average, thus allowing residents theoretically to return home. The decontamination work was also effective in limiting the migration of radiocesium in river systems because it targeted farmlands and residential areas concentrated in river valleys. These areas are the most sensitive to erosion, as they are the most connected to the river network (39). Furthermore, erosion of the topsoil layers ("inter-rill erosion") enriched in ^{137}Cs largely dominates in farmland and residential areas, which further explains the relevance of targeting these areas in priority for decontamination and the effectiveness of decontamination to reduce overall river ^{137}Cs fluxes. Accordingly, the results of the current research showed that ^{137}Cs activity concentrations in sediment transported in river systems draining the main radioactive pollution plume decreased by ca. 90% between 2011 and 2020 (22, 24, 25). In addition to these results, the modeling approach developed in this study showed that decontamination of 16% of the catchment surface area reduced the ^{137}Cs flux in rivers by 17% compared to estimates without decontamination. This modeling tool may be used to simulate management scenarios for hypothetical future crises.

The limited reduction in the ^{137}Cs inventory observed in Fukushima can mainly be explained by the absence of decontamination in forests, which cover ca. 80% of the landscape in this region. Interestingly, the current research demonstrates that contributions by forests occur mainly during typhoons, given the high

infiltration rates observed in forests that may be exceeded only during high cumulative rainfall (40, 41).

During these heavy rainfall events, the model showed that most sediments from forests are derived from rill and gully erosion processes in contrast to farmland and residential areas where topsoil (inter-rill) erosion dominates. Gully erosion on forested landscapes mobilizes subsoil layers that can be depleted in ^{137}Cs (42); this process explains why, even during typhoons, ^{137}Cs concentrations in the sediments transported by these rivers remain low after decontamination. Diffuse erosion in forests remains a permanent although limited source of ^{137}Cs because it only mobilizes very thin layers of soil and does not reach the maximum contamination depth.

Despite these considerations related to ^{137}Cs fluxes, the form of ^{137}Cs is also important, as the litter exported from forests may supply radioactive materials that are more bioavailable than those transported with mineral particles to downstream rivers and lakes (43–46). This was not incorporated in the current model version and could be included in future work.

Even if the transfer of ^{137}Cs across the landscape due to erosion and riverine transport is very limited now, 12 y after the accident, the fact that 67% of the ^{137}Cs stock remains stored under forests may represent a major obstacle for the return of the local population. Forests are ideal places for hiking, mushroom and plant foraging, hunting, and wood production (including harvesting logs from oak trees for shiitake cultivation). Many of these activities are now limited because these products have ^{137}Cs concentrations that are often above the limits set by the Japanese government (47). The impact of rill and inter-rill erosion in forests will likely continue to dilute ^{137}Cs in sediment exports, and ^{137}Cs concentration in forest products may eventually meet their respective guidelines.

The current research was particularly timely as it was conducted in an area representative of the conditions present across the entire Special Decontamination Area in which decontamination was completed early in 2017 (32). Across this area covering 1,117 km^2, 9,100,000 m^3 of waste was generated at a cost of 1.5 trillion yen [~12 billion euros or 10.7 million euros per km^2 (32)]. The removal of ^{137}Cs-contaminated soil following the Fukushima disaster appears to have been highly effective in reducing contamination in the treated areas and the river catchments draining these areas. However, due to the difficulty of removing contaminated soil from steep, forested slopes that cover nearly 84% of the affected catchment, the overall 17% reduction of ^{137}Cs fluxes was obtained after treating only 16% of the catchment area. The key question is, was the time, expense, and waste generated to restore 16% of the contaminated area worth the investment? As of 2019, 30% of the population returned to the region (48), which would not have been possible without the remediation effort. In any case, we hope that our results raise questions and lead to robust discussions among scientists, policy makers, and citizens about how to deal with potential nuclear fallout disasters in the future.

Materials and Methods

Materials and methods are summarized below, with details in *SI Appendix*.

Spatialized Data. A digital terrain model (DTM) derived from a light detection and ranging (LiDAR) survey with an initial resolution of 0.5 m was obtained and resampled to a 5 m grid. This model was then preprocessed following field observations of the runoff network to include small-scale features that may affect the runoff pathways (especially in relatively flat paddy-field regions with ditches).

The soil map was obtained from the National Agriculture and Food Research Organization (NARO) and is freely available at https://soil-inventory.rad.naro.go.jp/. The soils in the study area are mainly Cambisols (66%) and Andosols (21%). The soil map was reclassified to account for two soil groups: thick soils on hillslopes with low runoff potential (mainly forest soils) and soils in thalwegs and valley bottoms with higher runoff potential.

The land use map was based on data from the Japanese Ministry of Land, Infrastructure, Transport and Tourism, maps from the NARO (https://www.eorc.jaxa.jp/ALOS/en/dataset/lulc_e.htm) and visual observations from Google Maps (https://www.google.fr/maps). The Mano Dam catchment is mainly covered with forests (88.0%), residential areas (5.6%), agricultural land (3.3%), ponds and streams (2.3%), and roads (0.7%).

Rainfall Monitoring. The Fukushima Prefecture is equipped with multiple weather stations. Rainfall data were acquired at 10-min intervals, and one station (Maenori) is located in the Mano Dam catchment (37.73540N, 140.74257E). Data recorded at this station from June 2014 to December 2019 were used in this work. Some gaps in this record were filled with Automated Meteorological Data Acquisition System data from the nearest available station (Litate station: 37.655N, 140.72667E). Individual rainfall events were defined as periods in which more than 5 mm of rainfall accumulated, unbroken by a 3-h period devoid of precipitation. In total, 296 rainfall events were identified between June 2014 and December 2019.

Hydrological Monitoring. A hydrological station was installed immediately upstream of the Mano Dam Lake (Lake Hayama) in June 2014. The water height in the Mano River was measured using an AquiStar PT12 pressure/temperature sensor (INW, Kirkland, WA, USA) at 5-min intervals and then converted into flow rate data using gage curves. A 60- to 100-L river water sample was collected every 2 to 4 wk when the river conditions corresponded to the baseflow rate. Water and SS samples were also collected from the river section using an ISCO 6712 automatic water sampler (Teledyne Technologies, Lincoln, NE, USA) at 1 h intervals during flood events (see the following paragraph for the method for determining flood events). The SSC was determined in the laboratory by filtration using a Whatman GF/F filter with 0.7-µm pores (Cytiva, Tokyo, Japan), and these concentrations were then used to convert the turbidity logs measured by a DTS-12 digital turbidity sensor (FTS Inc., Victoria, BC CANADA) at 5-min intervals into SS logs. This station was damaged by Typhoon Etau in September 2015. Preliminary data analysis revealed some anomalies that persisted until the end of 2016 prompted us to omit the data acquired during this period. The hydrological station was subsequently moved a few hundred meters upstream in 2017. Water flows and SSC were subsequently acquired using the same systems described above at 10-min intervals until the end of 2019 (*SI Appendix*, Fig. S6).

Flood events were identified from continuous water measurements; the method employed (49) was based on the relative baseflow proportion, which was calculated using a recursive digital filter. Flood events were identified based on an established quick-flow/baseflow proportion threshold and were always associated with rainfall events. The baseflow was removed from the flood events before data processing. For each rainfall event, the following characteristics were calculated: the cumulative rainfall (mm), duration of rainfall (min), maximum intensity of rainfall (mm), antecedent rainfall in the previous 48 h (in mm), and cumulative rainfall since the previous event (mm). These parameters were associated with the characteristics of the corresponding flood event: the volume of water, mass of sediment, and quantity of ^{137}Cs. The volume was calculated by taking the integral of the flow curve. The mass was calculated as the product of the flow and SSC. The radiocesium flux per event was calculated following the same method as that used to reconstruct the high-frequency chronicles.

Radiocesium Measurements. For SS, river water samples collected during baseflow conditions were immediately passed through a nonwoven fabric cartridge filter with 1-µm pores (RP13-011; Japan Vilene, Tokyo, Japan) (50). Each cartridge filter with collected SS was dried at 105 °C for 24 to 48 h. The mass of SS attached to the cartridge was calculated by subtracting the dry weight of the sample filter from the dry weight of an unused filter. The particulate ^{137}Cs concentration in the SS (in Bq kg^{-1}) was calculated by dividing the amount of ^{137}Cs found in a cartridge filter with attached SS (in Bq) by the mass of SS attached to the cartridge filter (in kg). Turbid water samples (3 to 15 L) collected with an automatic water sampler under storm-runoff conditions were centrifuged at more than 5,000 rpm for 30 min, and the deposited sediment was then scraped off, packed in a U-8 container, and dried at 60 °C for at least 1 wk to obtain ^{137}Cs concentration per dry weight of SS.

The radiocesium activities (in Bq) of SS were determined using a GC2518 coaxial high-purity germanium detector (Canberra Japan, Tokyo, Japan) and a SEG-EMS GEM 35-70 coaxial high-purity germanium detector (Seiko EG&G, Tokyo, Japan) with Gammastudio software (Seiko EG&G). The radioisotope sources MX033U8PP (The Japan Radioisotope Association, Tokyo, Japan) and EG-ML (Eckert & Ziegler Isotope Products, Valencia, CA, USA) were used to calibrate the system. The cartridge filters were analyzed directly using the system following a method previously described by Tsuji et al. (2014) (50) (Fig. 2 and *SI Appendix*, Fig. S6).

Spatially Distributed Radiocesium Inputs. A FDNPP ^{137}Cs deposition map showing inventory values expressed in Bq m^{-2} was developed based on data collected during the third and fifth airborne surveys performed by the Ministry of Education, Culture, Sports, Science and Technology (29). This geospatial dataset was resampled to a resolution of 250 m (Fig. 1).

Radiocesium Outputs. Radiocesium concentrations in SS (Bq kg^{-1}) were obtained for 76 samples collected during baseflow conditions and 66 samples collected during flood events at the hydrological station. As most of the radiocesium fluxes occurred during flood conditions (51, 52), only the flood samples were considered when parameterizing the ^{137}Cs concentration decay trend over time.

To estimate these measured ^{137}Cs output fluxes, a chronology of particulate ^{137}Cs exports was reconstructed based on the relationship between ^{137}Cs concentrations (in Bq g^{-1}) in sediments during flood events as a function of time (Eq. **2**) and high-frequency flow and SSC measurements, in mg L^{-1}, during the corresponding period (Eq. **1**). These high-frequency radiocesium flux estimates were then integrated over the entire duration of the events to obtain the total flux (in Bq) exported during each event.

$$flux_{137Cs}(t) = Q \times SSC \times Conc_{137Cs}\,, \qquad [1]$$

with:

-$flux_{137Cs}$ (t): ^{137}Cs flux (Bq s^{-1})
-Q: flow rate (m^3 s^{-1})
-SSC: Suspended Sediment Concentration (mg L^{-1})
and:

$$Conc_{137Cs}(t) = a_1 \times e^{a_2 t}\,, \qquad [2]$$

with:

-$Conc_{137Cs}$: particulate ^{137}Cs concentration in SS (Bq g^{-1})
-t: elapsed time since the accident (years)
-a_1 and a_2: coefficients (cf. Fig. 2*A*)

Inventory/Mapping of Decontamination Operations. Spatially distributed data on the timing of decontamination operations in the Mano Dam catchment were provided by the Japanese Ministry of the Environment. The information was obtained from the National Institute for Environmental Science in the form of a file containing georeferenced points. Each point corresponded to an individual location within the residential areas, farmlands, grasslands, or roads where radiation dose rates were measured before and after decontamination occurred. The date of the last measurement was considered as the decontamination date. In addition, when forests were located within the vicinity of decontaminated areas, a buffer zone of 20 m was added, on the assumption that these zones were also remediated following the recommendations of the authorities. Finally, maps of decontaminated areas on a monthly scale between June 2014 and December 2016 were produced (*SI Appendix*, Fig. S7).

WaterSed Runoff and Erosion Modeling. The WaterSed model (37) is a non-dynamic distributed model that simulates runoff and soil erosion from the plot to the catchment scale during a sequence of rainfall events (34–36)–see *SI Appendix* for more details. In this work, runoff and erosion processes were calculated for a grid with a spatial resolution corresponding to that of the DTM (i.e., 5 m). Both the saturation-excess runoff and Hortonian overland flow were simulated. Both inter-rill and rill erosion phenomena were taken into account. The filling of the soil reservoir with water during rainfall and runoff processes remained in memory during the simulated sequence of rainfall events to describe the soil saturation conditions and the resulting runoff. Between events, this water stock was emptied using estimated seasonally variable evapotranspiration. A constant loss in the water storage layer was calibrated using one value per season: 0.5 mm d^{-1} during winter (December-March), 3 mm d^{-1} during spring (April–May), 6.5 mm d^{-1} during summer (June–September), and 2 mm d^{-1} during autumn (October-November). The relative amplitude for these values was chosen using the temperature variations. The absolute values were fixed during the calibration period. An antecedent soil moisture can then be determined before each event.

The model calculated several output maps for each event including those of runoff volume, sediment load, total gross erosion, inter-rill erosion, rill erosion, maximum flow rate, etc. These different maps provide useful tools for the spatial analysis of sediment sources for instance.

In total, 296 rainfall events were identified and modeled. Among these events, 48% had durations shorter than 5 h and cumulative rainfall totals of more than 7 mm. The events with cumulative rainfall totals higher than 100 mm corresponded to typhoons that occurred between the months of July and October (20).

Design of an Additional Radiocesium Module in the WaterSed Model. The assumptions of this module were the following:

-^{137}Cs is transported in particulate form only,
-^{137}Cs resulting from post-accident fallout was deposited "instantaneously" over soils at a constant thickness [approximately 2 cm (11)],
-the density of the soil is assumed to be constant at 1,400 kg m^{-3}, and
-the activity concentrations are decay-corrected to the date of the accident.

The additional input data included a map of the contaminated soil thicknesses ($e_{contaminated}$) (the initial thickness is constant over the contaminated area) and a ^{137}Cs soil concentration map (Bq kg^{-1}). As the ^{137}Cs deposition map was available in Bq m^{-2} (*Inventory*), it was converted into a concentration map (C_{137Cs}) with a spatial resolution corresponding to that of the DTM:

$$C_{137Cs} = \frac{Inventory}{e_{contaminated} \times density_{soil}}\,. \qquad [3]$$

Then, the activity map was decay-corrected:

$$C_{137Cs}^{t=1} = C_{137Cs}^{t=0} \times e^{-\lambda \times tps}\,, \qquad [4]$$

with,

$$\lambda = \frac{ln(2)}{t_{1/2}}\left(0.023 \times y^{-1}\right).$$

$t_{1/2}$: half-life of ^{137}Cs (30 y)
tps: time elapsed since the accident (years)

After each rainfall event was simulated, the resulting calculated erosion and deposition maps were used to update the contaminated soil thickness map and to calculate a sediment flux map, which was then used to derive the associated ^{137}Cs flux map. The ^{137}Cs soil concentration map was then recalculated after each event simulation, using the updated ^{137}Cs concentration and soil contaminated thickness maps.

In the sediment deposition areas, the updated contaminated soil thickness map was used to calculate an updated ^{137}Cs concentration while considering both the concentration in the deposited sediment layer and that in the underlying soil layer. This recalculated concentration was assumed to be homogeneous throughout the entire contaminated soil thickness (i.e., the mean concentration value was weighted based on the respective depths of these layers). In the erosion zones, the concentration was assumed to remain the same; only the available contaminated soil thicknesses changed. If the entire contaminated soil layer was eroded away and no sediment deposition occurred at that location, the ^{137}Cs concentration became zero (*SI Appendix*, Fig. S1).

Before the simulation of the subsequent rainfall event, the soil ^{137}Cs concentration was decay-corrected to the date of the next event:

$$C_{137Cs}^{t=i+1} = C_{137Cs}^{t=i}(1-\lambda \times \Delta t)\,. \qquad [5]$$

For locations affected by gully erosion or other forms of concentrated erosion in which features with widths lower than the mesh size (i.e., 5 m) are located, the

expedited depletion of the local ^{137}Cs contamination was calculated at each model run and remained in the model memory for the subsequent runs.

Model Calibration and Validation Datasets. The model was calibrated and validated on measured data between June 2014 and December 2019 (taking into account decontamination operations). Pedotransfer rules (e.g., the infiltration capacity, storage capacity, imbibition, erodibility, and potential sediment concentration) were assigned to units based on the soil and land use types in the study area. As cultivation was prohibited by the authorities after the accident, vegetation regrowth occurred very quickly following abandonment. This regrowth has been documented in the literature (23) using the normalized difference vegetation index. Thus, the soil cover properties in croplands were modified after abandonment, and these abandoned lands had intermediate infiltration capacities between those of regular croplands and grasslands. As these farmland soils were no longer plowed after the accident, the pedotransfer rules of the farmland did not change over time, except after decontamination operations began. Immediately after the decontamination operations started, the erodibility and potential SSC of farmlands increased (corresponding to sandy soil properties). Indeed, it was suggested in the literature that significant changes in erodibility may impact the catchment-scale sediment dynamics even if it occurs on a restricted size area (34). In contrast, the hydraulic properties of the decontaminated areas were not changed in the modeling because it was expected that variations in, for example, infiltration capacity on restricted size areas would not significantly impact the modeled water fluxes modeled at the catchment scale (35). During winter (November to February), it was assumed that vegetation did not grow, so areas decontaminated in winter were assumed to remain more erodible during this period. During the rest of the year, areas remained erodible for 2 mo before returning to their pre-decontamination state due to the rapid regrowth of vegetation. This rule was also applied to residential areas (including gardens) and grasslands.

The WaterSed model was calibrated by comparing the measured and simulated water volumes, peak flows, and SS at the catchment outlet corresponding to a selection of 21 significant rainfall events that occurred between June 2014 and September 2015. The calibration results were then evaluated using the coefficient of determination (R^2), Nash–Sutcliffe index (Nash), percentage bias |PBIAS|, and Root Mean Square Erorr (RMSE) (*SI Appendix*, Fig. S2). In addition, the pedotransfer rules were adjusted by comparing the modeled sediment fluxes and runoff coefficients for each land cover type with values from the literature (4, 13, 16, 53). The parameters retained were those that achieved the best performance criteria. The Nash for the model outputs (water volumes, peak flows, and SS) varied between 0.62 and 0.75 and the |PBIAS| values remained lower than 0.7% (*SI Appendix*, Fig. S2). Consequently, the quality of the calibration was assessed to be good to very good (54). The model underestimates the water volumes (*SI Appendix*, Fig. S2*A*) by about 17% but reproduces well on average the peak flows (R^2 = 0.62 and Nash = 0.44) and the sediment load flows (R^2 = 0.75 and Nash = 0.70) (Fig. 2*C* and *B*). Although there was some scattering when comparing the model outputs to monitoring measurements, the R^2 and RMSE values obtained indicate that the model adequately reproduced the catchment water and sediment dynamics (*SI Appendix*, Figs. S2 and S4).

Once runoff and erosion were calibrated, the radiocesium module was calibrated. The timing of decontamination shown by the monthly decontamination maps described above was used to progressively update the ^{137}Cs concentration and contaminated soil thickness maps as well as the factors controlling erosion in the model.

It was assumed that in the decontaminated areas, the ^{137}Cs concentration in sediment was reduced by 80%, and the contaminated thickness was 5 cm. This value was chosen in accordance with the official decontamination protocol, which consisted of removing the upper few cm of soil and adding mixed crushed granite to a depth of 5 cm (32).

The radiocesium module was calibrated by testing multiple contaminated soil depths (between 1.5 and 2.5 cm at every 0.01-cm increment). Each tested depth was then evaluated by comparing the modeled radiocesium fluxes with those estimated from the point-based measurements recorded at the outlet. The best results obtained for the ^{137}Cs fluxes at the outlet were obtained for a soil contamination depth of 2.2 cm with a R^2 of 0.84 and a Nash of 0.80 (*SI Appendix*, Fig. S2*D*). The low magnitude events are overestimated, which can be attributed to the flux reconstruction method (as the proportion of bias introduced is higher on low fluxes).

An extensive set of 103 events occurring between June 2014 and December 2019 was used for validation. The events used for model calibration included cumulative rainfall amounts ranging from 7 to 120 mm and durations ranging from a few minutes to 5 h. These events therefore effectively covered the range of events used in the validation step (*SI Appendix*, Fig. S3). This validation demonstrates the good quality of model predictions for both sediment (R^2 = 0.79; Nash = 0.68) and ^{137}Cs fluxes (R^2 = 0.80; Nash = 0.69) mainly for the heaviest events that supplied most of the flux (*SI Appendix*, Fig. S4). In contrast, more scattering is observed for the lowest intensity events due to their high variability, although they contribute only to a minor proportion of the flux.

Quantification of the Impact of Decontamination. To quantify the effects of decontamination, all rainfall events that occurred between June 2014 and December 2019 were simulated without decontamination by not modifying the pedotransfer rules in the decontaminated areas. As WaterSed is an event-based model, its results were compared with the data resulting from ^{137}Cs concentration monitoring carried out until the end of 2019 following two methods: i) comparison of modeled concentration values with the measured concentrations and ii) comparison of modeled ^{137}Cs fluxes per event with the fluxes estimated from the measured point-based concentrations. The results of each simulation were then used to calculate the evolution of the ^{137}Cs stock in the catchment area as a function of time.

Data, Materials, and Software Availability. Monitoring data have been deposited in Zenodo (30). All other data are included in the article and/or *SI Appendix*.

ACKNOWLEDGMENTS. This research was funded by the AMORAD (ANR-11-RSNR-0002) project (ANR, Agence Nationale de la Recherche, Programme des Investissements d'Avenir). The support of the CNRS International Research Project–IRP–MITATE Lab is also gratefully acknowledged. This work was also supported by the Environmental Radioactivity Research Network Center through grants I-21-22 and I-22-24. We acknowledge Y. Onda for providing LiDAR data produced by the Geographical Institute of Japan. We would like to thank the two anonymous reviewers for their constructive comments which helped us to improve this paper.

Author affiliations: [a]Risk and Prevention Division, Bureau de Recherches Géologiques et Minières (BRGM), F-45060, Orléans, France; [b]Fukushima Regional Collaborative Research Center, National Institute for Environmental Science, Miharu, Tamura, Fukushima 963-7700, Japan; [c]Laboratoire des Sciences du Climat et de l'Environnement (LSCE), Institut Pierre Simon Laplace (IPSL), Unité Mixte de Recherche 8212 Commissariat à l'Énergie Atomique et aux Énergies Alternatives (CEA), CNRS, Université de Versailles Saint-Quentin (UVSQ), Université Paris-Saclay, Gif-sur-Yvette F-91191, France; [d]Airshed and Watershed Stewardship Branch, Environment and Protected Areas, Government of Alberta, Calgary, AB T2L 2K8, Canada; and [e]Radioisotope Geoscience Division, Institute of Environmental Radioactivity, University of Fukushima, Fukushima 960-1296, Japan

1. J. Groëll, D. Quélo, A. Mathieu, Sensitivity analysis of the modelled deposition of 137 Cs on the Japanese land following the Fukushima accident. *Int. J. Environ. Pollut.* **55**, 67–75 (2014).
2. H. Kawamura *et al.*, Preliminary numerical experiments on oceanic dispersion of 131 I and 137Cs discharged into the ocean because of the Fukushima Daiichi Nuclear Power Plant disaster. *J. Nucl. Sci. Technol.* **48**, 1349–1356 (2011).
3. T. Kobayashi, H. Nagai, M. Chino, H. Kawamura, Source term estimation of atmospheric release due to the Fukushima Dai-ichi Nuclear Power Plant accident by atmospheric and oceanic dispersion simulations. *J. Nucl. Sci. Technol.* **50**, 255–264 (2013).
4. A. Kitamura, M. Yamaguchi, H. Kurikami, M. Yui, Y. Onishi, Predicting sediment and cesium-137 discharge from catchments in eastern Fukushima. *Anthropocene* **5**, 22–31 (2014).
5. K. Saito *et al.*, Detailed deposition density maps constructed by large-scale soil sampling for gamma-ray emitting radioactive nuclides from the Fukushima Dai-ichi Nuclear Power Plant accident. *J. Environ. Radioact.* **139**, 308–319 (2015).
6. Q. He, D. E. Walling, Interpreting particle size effects in the adsorption of 137Cs and unsupported 210Pb by mineral soils and sediments. *J. Environ. Radioact.* **30**, 117–137 (1996).
7. B. L. Sawhney, Selective sorption and fixation of cations by clay minerals: A review. *Clays Clay Miner.* **20**, 93–100 (1972).
8. T. Tamura, Consequences of activity release: Selective sorption reactions of cesium with soil minerals. *Nucl. Saf.* **5**, 262–268 (1964).
9. S. Shiozawa, "Vertical migration of radiocesium fallout in soil in Fukushima" in *Agricultural Implications of the Fukushima Nuclear Accident*, T. M. Nakanishi, K. Tanoi, Eds. (Springer, Japan, 2013), pp. 49–60.
10. A. Nakao, S. Ogasawara, O. Sano, T. Ito, J. Yanai, Radiocesium sorption in relation to clay mineralogy of paddy soils in Fukushima, Japan. *Sci. Total Environ.* **468–469**, 523–529 (2014).
11. H. Lepage *et al.*, Depth distribution of cesium-137 in paddy fields across the Fukushima pollution plume in 2013. *J. Environ. Radioact.* **147**, 157–164 (2015).

12. V. Yoschenko *et al.*, Late phase radiocesium dynamics in fukushima forests post deposition. *J. Environ. Radioact.* **251–252**, 106947 (2022).
13. K. Osawa *et al.*, Quantification of dissolved and particulate radiocesium fluxes in two rivers draining the main radioactive pollution plume in Fukushima, Japan (2013–2016). *Anthropocene* **22**, 40–50 (2018).
14. Y. Yamashiki *et al.*, Initial flux of sediment-associated radiocesium to the ocean from the largest river impacted by Fukushima Daiichi Nuclear Power Plant. *Sci. Rep.* **4**, 1–7 (2014).
15. M. Yamaguchi, A. Kitamura, Y. Oda, Y. Onishi, Predicting the long-term 137Cs distribution in Fukushima after the Fukushima Dai-ichi nuclear power plant accident: A parameter sensitivity analysis. *J. Environ. Radioact.* **135**, 135–146 (2014).
16. K. Yoshimura, Y. Onda, H. Kato, Evaluation of radiocaesium wash-off by soil erosion from various land uses using USLE plots. *J. Environ. Radioact.* **139**, 362–369 (2015).
17. O. Evrard *et al.*, Radiocesium transfer from hillslopes to the Pacific Ocean after the Fukushima Nuclear Power Plant accident: A review. *J. Environ. Radioact.* **148**, 92–110 (2015).
18. A. Kitamura *et al.*, Redistribution and export of contaminated sediment within eastern Fukushima Prefecture due to typhoon flooding. *Earth Surf. Process. Landforms* **41**, 1708–1726 (2016).
19. J. P. Laceby *et al.*, Rainfall erosivity in catchments contaminated with fallout from the Fukushima Daiichi Nuclear Power Plant accident. *Hydrol. Earth Syst. Sci.* **20**, 2467–2482 (2016).
20. J. P. Laceby, S. Huon, Y. Onda, V. Vaury, O. Evrard, Do forests represent a long-term source of contaminated particulate matter in the Fukushima Prefecture? *J. Environ. Manage.* **183**, 742–753 (2016).
21. O. Evrard *et al.*, Research and management challenges following soil and landscape decontamination at the onset of the reopening of the Difficult-to-Return Zone, Fukushima (Japan). *SOIL* **9**, 479–497 (2023).
22. O. Evrard *et al.*, Radionuclide contamination in flood sediment deposits in the coastal rivers draining the main radioactive pollution plume of Fukushima Prefecture, Japan (2011–2020). *Earth Syst. Sci. Data* **13**, 2555–2560 (2021).
23. B. Feng *et al.*, Persistent impact of Fukushima decontamination on soil erosion and suspended sediment. *Nat. Sustain.* **5**, 879–889 (2022), 10.1038/s41893-022-00924-6.
24. S. Ueda, H. Hasegawa, Y. Ohtsuka, S. Ochiai, T. Tani, Ten-year radiocesium fluvial discharge patterns from watersheds contaminated by the Fukushima nuclear power plant accident. *J. Environ. Radioact.* **240**, 106759 (2021).
25. K. Taniguchi *et al.*, Transport and redistribution of radiocesium in Fukushima fallout through rivers. *Environ. Sci. Technol.* **53**, 12339–12347 (2019).
26. T. Kinouchi, K. Yoshimura, T. Omata, Modeling radiocesium transport from a river catchment based on a physically-based distributed hydrological and sediment erosion model. *J. Environ. Radioact.* **139**, 407–415 (2015).
27. K. Sakuma *et al.*, Evaluation of sediment and 137Cs redistribution in the Oginosawa River catchment near the Fukushima Dai-ichi Nuclear Power Plant using integrated watershed modeling. *J. Environ. Radioact.* **182**, 44–51 (2018).
28. C. Chartin *et al.*, Tracking the early dispersion of contaminated sediment along rivers draining the Fukushima radioactive pollution plume. *Anthropocene* **1**, 23–34 (2013).
29. H. Kato, Y. Onda, X. Gao, Y. Sanada, K. Saito, Reconstruction of a Fukushima accident-derived radiocesium fallout map for environmental transfer studies. *J. Environ. Radioact.* **210**, 105996 (2019).
30. S. Hayashi *et al.*, River monitoring, particulate Cs-137 measurements and rainfall monintoring of the Mano Dam catchment (Japan). https://doi.org/10.5281/ZENODO.7886524 (3 May 2023).
31. M. Sakai, T. Gomi, M. Nunokawa, T. Wakahara, Y. Onda, Soil removal as a decontamination practice and radiocesium accumulation in tadpoles in rice paddies at Fukushima. *Environ. Pollut.* **187**, 112–115 (2014).
32. O. Evrard, J. Patrick Laceby, A. Nakao, Effectiveness of landscape decontamination following the fukushima nuclear accident: A review. *Soil* **5**, 333–350 (2019).
33. O. Navratil *et al.*, Global uncertainty analysis of suspended sediment monitoring using turbidimeter in a small mountainous river catchment. *J. Hydrol.* **398**, 246–259 (2011).
34. T. Grangeon, R. Vandromme, O. Cerdan, A. M. De Girolamo, A. Lo Porto, Modelling forest fire and firebreak scenarios in a mediterranean mountainous catchment: Impacts on sediment loads. *J. Environ. Manage.* **289**, 112497 (2021).
35. J. E. M. Baartman *et al.*, What do models tell us about water and sediment connectivity? *Geomorphology* **367**, 107300 (2020).
36. E. Patault *et al.*, Predicting sediment discharge at water treatment plant under different land use scenarios coupling expert-based GIS model and deep neural network. *Hydrol. Earth Syst. Sci. Discuss.* **25**, 6223–6238 (2021).
37. V. Landemaine *et al.*, Saturation-excess overland flow in the European loess belt: An underestimated process? *Int. Soil Water Conserv. Res.* **11**, 688–699 (2023).
38. Y. Wakiyama, Y. Onda, S. Mizugaki, H. Asai, S. Hiramatsu, Soil erosion rates on forested mountain hillslopes estimated using 137Cs and 210Pbex. *Geoderma* **159**, 39–52 (2010).
39. C. Chartin *et al.*, The impact of typhoons on sediment connectivity: Lessons learnt from contaminated coastal catchments of the Fukushima Prefecture (Japan). *Earth Surf. Process. Landforms* **42**, 306–317 (2017), 10.1002/esp.4056.
40. S. Miyata *et al.*, Assessing spatially distributed infiltration capacity to evaluate storm runoff in forested catchments: Implications for hydrological connectivity. *Sci. Total Environ.* **669**, 148–159 (2019).
41. K. Nanko *et al.*, Variability of surface runoff generation and infiltration rate under a tree canopy: Indoor rainfall experiment using Japanese cypress (Chamaecyparis obtusa). *Hydrol. Process. Hydrol. Process* **24**, 567–575 (2010).
42. T. Fukuyama *et al.*, Quantifying the impact of forest management practice on the runoff of the surface-derived suspended sediment using fallout radionuclides. *Hydrol. Process. Hydrol. Process* **24**, 596–607 (2010).
43. H. Funaki *et al.*, Remobilisation of radiocaesium from bottom sediments to water column in reservoirs in Fukushima, Japan. *Sci. Total Environ.* **812**, 152534 (2022).
44. S. Hayashi, H. Tsuji, I. Yumiko, Effects of forest litter on dissolved 137Cs concentrations in a highly contaminated mountain river in Fukushima. *J. Hydrol. Reg. Stud.* **41**, 101099 (2022).
45. A. Zimmermann, T. Francke, H. Elsenbeer, Forests and erosion: Insights from a study of suspended-sediment dynamics in an overland flow-prone rainforest catchment. *J. Hydrol.* **428–429**, 170–181 (2012).
46. T. Oda *et al.*, Redistribution of the soil 137 Cs inventory through litter and sediment transport on a hillslope covered by deciduous forest in Fukushima, Japan. *Earth Surf. Process. Landforms* **47**, 2531–2543 (2022).
47. S. Hashimoto, M. Komatsu, S. Miura, *Forest Radioecology in Fukushima* (Springer Singapore, 2022), 10.1007/978-981-16-9404-2.
48. C. Asanuma-Brice, O. Evrard, T. Chalaux, Why did so few refugees return to the Fukushima fallout-impacted region after remediation? An interdisciplinary case study from Iitate village Japan. *Int. J. Disaster Risk Reduct.* **85**, 103498 (2023).
49. T. Grangeon *et al.*, Hydro-sedimentary dynamics of a drained agricultural headwater catchment: A nested monitoring approach. *Vadose Zo. J.* **16**, 1–11 (2017).
50. H. Tsuji, Y. Kondo, S. Kawashima, T. Yasutaka, Non-destructive detection of particulate radiocesium using a non-woven fabric cartridge filter for rapid preprocessing. *J. Radioanal. Nucl. Chem.* **303**, 1803–1810 (2015).
51. O. Evrard *et al.*, Quantifying the dilution of the radiocesium contamination in Fukushima coastal river sediment (2011–2015). *Sci. Rep.* **6**, 34828 (2016).
52. S. Huon *et al.*, Source dynamics of radiocesium-contaminated particulate matter deposited in an agricultural water reservoir after the Fukushima nuclear accident. *Sci. Total Environ.* **612**, 1079–1090 (2018).
53. Y. Wakiyama, Y. Onda, K. Yoshimura, Y. Igarashi, H. Kato, Land use types control solid wash-off rate and entrainment coefficient of Fukushima-derived 137Cs, and their time dependence. *J. Environ. Radioact.* **210**, 105990 (2019).
54. D. N. Moriasi *et al.*, Model evaluation guidelines for systematic quantification of accuracy in watershed simulations. *Trans. ASABE* **50**, 885–900 (2007).